Showcasing research from Professor Arčon's and Professor Prassides' laboratories, Jožef Stefan Institute, Ljubljana, Slovenia and Department of Physics, Osaka Metropolitan University, Osaka, Japan.

Fulleride superconductivity tuned by elastic strain due to cation compositional disorder

Beyond bandwidth-controlled superconductivity: cation structural-disorder in the tetrahedral sites of face-centred-cubic–structured alkali-intercalated fullerides finely tunes their superconducting properties at the same bandwidth.

ROYAL SOCIETY
OF **CHEMISTRY**

rsc.li/chemical-science

EDGE ARTICLE

Check for updates

All publication charges for this article have been paid for by the Royal Society of Chemistry

Fulleride superconductivity tuned by elastic strain due to cation compositional disorder†

H. Esma Okur, [ID] [a] Ross H. Colman, [ID] [b] Yasuhiro Takabayashi, [ID] [c] Peter Jeglič, [ID] [d] Yasuo Ohishi, [e] Kenichi Kato, [f] Denis Arčon, [ID] [dg] Yoshiki Kubota [h] and Kosmas Prassides [ID] *[dhi]

Dynamical fluctuations of the elastic strain in strongly correlated systems are known to affect the onset of metal-to-insulator or superconducting transitions. Here we report their effect on the properties of a family of bandwidth-controlled alkali-intercalated fullerene superconductors. We introduce elastic strain through static local structural disorder in a systematic and controllable way in the fcc-structured $K_xCs_{3-x}C_{60}$ (with potassium content, $0.22 \leq x_K \leq 2$) series of compositions by utilizing the difference in size between the K^+ and Cs^+ co-dopants. The occurrence of the crossover from the Mott–Jahn–Teller insulating (MJTI) state into the strongly correlated Jahn–Teller metal (JTM) on cooling is evidenced for the compositions with $x_K < 1.28$ by both synchrotron X-ray powder diffraction (SXRPD) – anomalous reduction of the unit cell volume – and ^{133}Cs NMR spectroscopy – sudden suppression in the ^{133}Cs spin-lattice relaxation rates. The emerging superconducting state with a maximum critical temperature, $T_c = 30.9$ K shows a characteristic dome-like dependence on the unit-cell volume or equivalently, on the ratio between the on-site Coulomb repulsion, U, and the bandwidth, W. However, compared to the parent Cs_3C_{60} composition in which cation disorder effects are completely absent, the maximum T_c is lower by ~12%. The reduction in T_c displays a linear dependence on the variance of the tetrahedral-site cation size, σ_T^2, thus establishing a clear link between structural-disorder–induced attenuation of critical elastic strain fluctuations and the electronic ground state.

1 Introduction

Superconductors in which the electronically active units are molecules rather than atoms typically incorporate π-electron open-shell units. Among the members of the family of

[a]Department of Chemistry, Faculty of Engineering and Natural Sciences, Bursa Technical University, TR-16310 Bursa, Turkey

[b]Department of Condensed Matter Physics, Faculty of Mathematics and Physics, Charles University, 121 16 Prague, Czech Republic

[c]Department of Physical Science and Engineering, Nagoya Institute of Technology, Nagoya 466-8555, Japan

[d]Jozef Stefan Institute, Jamova c. 39, SI-1000 Ljubljana, Slovenia

[e]Japan Synchrotron Radiation Facility, SPring-8, Hyogo 679-5198, Japan

[f]RIKEN SPring-8 Center, Hyogo 679-5148, Japan

[g]Faculty of Mathematics and Physics, University of Ljubljana, Jadranska c. 19, SI-1000 Ljubljana, Slovenia

[h]Department of Physics, Graduate School of Science, Osaka Metropolitan University, Osaka 599-8531, Japan. E-mail: k.prassides@omu.ac.jp

[i]Faculty of Engineering, Kyoto University of Advanced Science, Kameoka 621-8555, Japan

† Electronic supplementary information (ESI) available: Additional details of the experimental methods; tables of the refined parameters of the Rietveld analysis results of the synchrotron X-ray diffraction data at ambient and elevated pressures (Tables S1–S14); figures of the Rietveld fits of the diffraction data, of additional NMR spectral information, and of magnetic susceptibility data (Fig. S1–S26). See DOI: https://doi.org/10.1039/d4sc03399j

molecular superconductors, the trivalent alkali fullerides, A_3C_{60} (A = alkali metal) are best-in-class representatives exhibiting the highest superconducting transition temperature, T_c (at 38 K under applied pressure)[1] and with their zero-resistance state surviving to extremely high magnetic fields ($H_{c2} > 90$ T).[2] Very importantly, it has been also established that electron correlations play a dominant role in the superconducting pairing mechanism, thereby rendering these materials members of the family of unconventional high-T_c superconductors.[3–7]

All studies reported so far attest that the transitions between the various electronic states of the A_3C_{60} fullerides are achieved principally *via* altering the interfullerene separation, which modifies the size of the bandwidth, W, and therefore tunes the ratio (U/W), where U is the on-site Coulomb repulsion.[8] For molecular systems like the A_3C_{60} fullerides, U is on the order of 1 eV and varies little across the various compositions.[5–7] The parent hyperexpanded compound Cs_3C_{60}, in which (U/W) is maximal, is a magnetic insulator at ambient pressure and crystallizes as either the A15-structured (primitive cubic phase comprising orientationally ordered C_{60}^{3-} units) or the fcc-structured (face-centred cubic phase comprising merohedrally disordered C_{60}^{3-} units) polymorph.[3,4] Application of physical pressure to both polymorphs suppresses the magnetic state leading to a Mott-insulator-to-metal transition as the

interfullerene separation is reduced, W increases, and (U/W) shifts below a critical value. Upon cooling, superconductivity emerges from the metallic state with a dome-shaped dependence of T_c with volume, V, occupied per C_{60}^{3-} anion.[1,3,4,8–10] The maximum T_c is somewhat higher for the A15 Cs_3C_{60} phase at 38 K compared to the value measured for the fcc Cs_3C_{60} phase (35 K).

However, while the A15 structure is encountered only at the high-packing densities of the parent Cs_3C_{60} phase, the fcc-structured A_3C_{60} phases are stable over a broad range of packing densities, and therefore (U/W) ratios. As a result, application of physical and/or chemical pressure to the most expanded fcc-structured Cs_3C_{60} phase has allowed the exploration of the electronic phase diagram of the fullerides in great detail.[11–18] Firstly, as the orbital overlap of neighbouring C_{60}^{3-} anions increases upon pressurisation, the MJTI state is destroyed. The metallic state, which emerges from the insulator is unconventional and is characterized by fluctuating microscopically heterogeneous co-existence of both localized Jahn–Teller-active and itinerant electrons (JTM). Further pressurization, leads to the gradual disappearance of localised Jahn–Teller features and the evolution of the unconventional JTM to a conventional Fermi liquid. At the same time, the s-wave superconducting state evolves from an unconventional correlated superconductor in the strong-coupling limit to a weak-coupling BCS-like superconductor. Notably, the JTM is the parent state of the unconventional fulleride superconductor with the highest T_c encountered at the crossover between JTM and Fermi liquid behaviour.[11]

Manipulation of the fcc-structured Cs_3C_{60} phase by chemical pressure was successfully achieved by altering the cation occupation of the tetrahedral (T) interstitial sites, which are smaller ($r_T = 1.12$ Å) than the ionic size of the heavier alkali dopants (K^+, Rb^+, and Cs^+). As a result, fulleride packing density can be sensitively controlled by the occupation of the tetrahedral sites as the proportions of isovalent K^+, Rb^+, and Cs^+ ions vary. Increased amounts of the smaller size ions lead to lattice contraction, increased values of W, and smaller values of (U/W).[11] On the other hand, the occupancy of the octahedral (O) sites by different alkali ions plays a minor role as the hole size ($r_O = 2.06$ Å) is larger than the ionic radius of all alkali ions. The detailed investigation of the chemical pressure effect across the fcc-structured members of the $Rb_xCs_{3-x}C_{60}$ ($0.35 \leq x \leq 2$) series revealed the existence of an electronic phase diagram entirely comparable to that established upon physical pressurization of the parent Cs_3C_{60} phase.[11] This is consistent with the dominant role of the intermolecular overlaps in controlling the magnetic and metallic/superconducting states of the materials.[3,4] Notably, however, these studies revealed a small but significant ($\sim$5%) reduction of the maximum T_c, which appears smaller (33.2 K) in the chemically pressurized analogues when compared to physically pressurized Cs_3C_{60} (35.1 K). This T_c reduction is evident at all packing densities, V despite the expected identical values of the bandwidth, W and the corresponding (U/W) ratios.

This observation necessitates a revisit of the role of the alkali ions in determining the superconducting properties of the fulleride phases. In particular, there is a well-defined difference in the occupation of the tetrahedral interstices in the Rb_x-$Cs_{3-x}C_{60}$ ($0 \leq x \leq 3$) phase field: when $x = 0$, 2, and 3, the tetrahedral holes are occupied by either Cs^+ or Rb^+ alone, while for all other values of x, they are occupied by a disordered mixture of Rb^+ and Cs^+ cations. Such disorder of cation occupation of available structural cavities and the associated cooperative fluctuations of the elastic strain generated have been shown before to influence sensitively a variety of electronic responses[19] including metal-insulator and superconducting transitions in strongly correlated transition metal oxide phases such as the magnetoresistive manganites[20] and the high-T_c cuprates,[21] respectively.

This raises the issue whether the generic nature of such elastic interactions is also relevant to the electronic properties of fulleride superconductors and could be responsible for the small, but significant, suppression in the magnitude of their T_c encountered when cation disorder is present. Here, we undertake a systematic study of the structural and electronic properties of the series of fcc-structured $K_xCs_{3-x}C_{60}$ (with nominal content, $0.12 \leq x \leq 2$) fullerides at both ambient and elevated pressures. Due to the increased difference in size between the K^+ and Cs^+ constituent ions, we are able to enhance further the ionic size effects, culminating in even larger suppression (on the order of 12%) of the values of T_c observed in the absence of disorder at the same fulleride packing density. The high quality of the experimental data allowed us to establish quantitatively the effects of cation disorder and the associated cooperative elastic interactions on T_c.

2 Materials and methods

2.1 Synthesis and characterisation

Polycrystalline $K_xCs_{3-x}C_{60}$ (nominal K content, $0.12 \leq x \leq 2$) compounds were synthesized by high-temperature reactions of stoichiometric quantities of sublimed C_{60} and phase-pure K_6C_{60} and Cs_6C_{60} precursors (Fig. S1†). The exact experimental protocol is detailed in the ESI.† As small amounts of reactants are employed in these preparations, the use of free-flowing A_6C_{60} (A = K, Cs) powders instead of K and Cs metals allows better stoichiometry control of the target compositions. Due to the extreme air- and moisture-sensitivity, all sample manipulations were carried out in an Ar-filled glove box. Laboratory X-ray powder diffraction (Bruker D8 Advance, Debye–Scherrer geometry, CuK$_{\alpha 1}$ radiation, $\lambda = 1.54056$ Å) was used to monitor the quality of all intermediate and the final polycrystalline products. Samples were obtained as free-flowing black-coloured powders.

2.2 Structural measurements at ambient and elevated pressures

High-resolution synchrotron X-ray powder diffraction (SXRPD) measurements of the samples at ambient pressure were performed using a helium-flow cryostat between 10 and 300 K with the multidetector diffractometer on beamline ID31 and ID22 ($\lambda \sim$ in the range 0.35 to 0.4 Å) at the European Synchrotron

Radiation Facility (ESRF), Grenoble, France. Data for the $x = 1$ sample were obtained between 112 and 300 K with the diffractometer on beamline BL44B2 ($\lambda = 0.81887$ Å) at SPring-8, Japan.[22] Pressure-dependent high-resolution SXRPD data ($\lambda \sim 0.41$ Å) were collected at 7 K for samples of nominal composition $K_xCs_{3-x}C_{60}$ ($x = 0.25, 0.75, 1$) at pressures between 0.2 and 10 GPa on beamline BL10XU, SPring-8, Japan. Data analysis of the SXRPD profiles at both ambient and elevated pressures was performed with the GSAS suite of Rietveld analysis programs.[23]

2.3 Magnetic measurements at ambient and elevated pressures

Ambient-pressure magnetic measurements were carried out with a Quantum Design SQUID MPMS magnetometer on $\sim$20–25 mg powder samples loaded in thin-walled quartz ampoules and sealed under a He gas partial pressure ($\sim$300 mbar). The magnetization, M, of all samples was measured at an applied field of either 10 or 20 Oe between 1.8 and 40 K under both zero-field-cooled (ZFC) and field-cooled (FC) protocols. Temperature-dependent magnetic susceptibility, χ, data were also collected at 3 and 5 T under FC protocols between 1.8 and 300 K. High-pressure magnetization measurements at 20 Oe under ZFC protocols were carried out under applied pressures of up to 10.3 kbar with an easyLab Technologies piston-cylinder high-pressure cell (Mcell 10). High-purity Sn was used as an *in situ* manometer with Daphne mineral oil as the pressure transmitting medium.

2.4 NMR spectroscopy

^{133}Cs (spin $I = 7/2$) and ^{39}K NMR (spin $I = 3/2$) spectra and spin-lattice relaxation, T_1, times were measured for $K_xCs_{3-x}C_{60}$ [nominal content, $x = 0.35, 0.5, 2$; refined content, $x_K = 0.53$, 0.64, 2 (*vide infra*)] powders at a magnetic field of 9.39 T. Samples were sealed into Pyrex glass tubes under a low-pressure He atmosphere. Measurements were conducted between 4 and 420 K in a liquid He flow cryostat with a temperature stability better than ± 0.1 K over the entire temperature range. As a ^{133}Cs NMR reference, a $CsNO_3$ standard was used with a corresponding reference frequency, $\nu_{ref}(^{133}Cs) = 52.4609$ MHz. In the ^{133}Cs NMR experiments, a solid-echo pulse sequence (β)–τ–(β)–τ–echo was used with a pulse length, $\tau(\beta) = 4$ μs, an interpulse delay, $\tau = 50$ μs and appropriate phase cycling. The same pulse sequence was also used to detect the ^{39}K NMR signal (KCl standard, $\nu_{ref}(^{39}K) = 18.6633$ MHz) but with a larger pulse width of 14 μs and an interpulse delay, τ of 200 μs. For spin-lattice relaxation measurements, the inversion recovery technique was applied in both cases.

As the $K_xCs_{3-x}C_{60}$ phase assemblages might contain Cs_4C_{60} and/or CsC_{60} impurity phases (*vide infra*), we employed a similar strategy as in our earlier work on overexpanded Cs_3C_{60} samples[3,4] in order to relatively enhance the ^{133}Cs NMR signal arising from the fcc phases. The symmetry of the Cs^+ sites of the Cs_4C_{60} phase is lower than axial (point group C_{2v}), leading to broadening of the respective NMR spectral lines by quadrupole interactions. As a result, such lineshape broadening together with the low phase concentration, and the experimental pulse-

length optimization for the fcc Cs_3C_{60} phase suppress the Cs_4C_{60} contribution to the NMR signal amplitude.[3,4] In addition, the ^{133}Cs NMR signal of the CsC_{60} impurity is shifted by $\sim$800 ppm relative to the reference and is thus well separated from the main O- and T-site signals. Indeed, while the ^{133}Cs NMR signal of the CsC_{60} impurity is detected in Cs_3C_{60} samples,[3,4] it is too low in intensity to be observed in the K_x-$Cs_{3-x}C_{60}$ series (Fig. S2†).

3 Results

3.1 Structural evolution of $K_xCs_{3-x}C_{60}$ at ambient and elevated pressures

A series of eight $K_xCs_{3-x}C_{60}$ samples with nominal x varying between 0.12 and 2 were synthesized. Inspection of their high-resolution SXRPD profiles (Fig. S3†) collected at ambient temperature reveals in all cases the formation of cubic fulleride phases with fcc symmetry (Fig. 1a) and with an increasing lattice size, a as the content of the smaller K^+ cation, x decreases. At the same time, the purity of the samples degrades with increasing Cs^+ content – decreasing x – as the fractions of co-existing Cs_4C_{60} and CsC_{60} phases grow at the expense of that of the
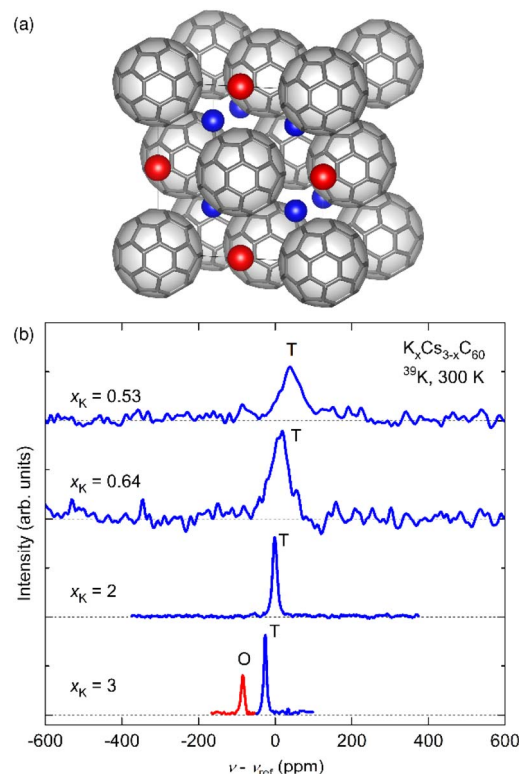

Fig. 1 (a) Crystal structure of fcc fullerides (space group $Fm\bar{3}m$) with stoichiometry A_3C_{60} (A is an alkali metal cation; blue spheres depict cations residing in tetrahedral (T) and red in octahedral (O) interstices, respectively). The C_{60}^{3-} units are merohedrally disordered; here only one of the two possible orientations is depicted at each lattice position. (b) ^{39}K NMR spectra measured for $K_{3-x}Cs_xC_{60}$ (refined $x_K = 0.53$, 0.64, 2, 3) powders at 300 K. The T and O peaks are labelled in blue and red colour, respectively. The spectrum of $K_{3-x}Cs_xC_{60}$ ($x = 3$) is been reproduced from ref. 24.

fcc-structured phases. As established before, both fcc Cs_3C_{60} (ref. 4) and the expanded fcc fullerides $Rb_xCs_{3-x}C_{60}$ (ref. 11) are not accessible in phase-pure form due to the competing disproportionation reaction into CsC_{60} and Cs_4C_{60} – driven by the size mismatch between the large Cs^+ and Rb^+ cations and the small tetrahedral fcc interstitial sites – that leads to the isolation of three-phase assemblages. Rietveld analysis of the SXRPD data was undertaken by employing the established merohedrally disordered fulleride model (space group $Fm\bar{3}m$) for the fcc-structured components.

An important issue which arises from the different size of the octahedral ($r_O = 2.06$ Å) and tetrahedral ($r_T = 1.12$ Å) cavities in the fcc unit cell relates to their possible preferred occupation by the larger Cs^+ ($r_{Cs^+} = 1.67$ Å) and smaller K^+ ($r_{K^+} = 1.38$ Å) ions, respectively. This can be addressed experimentally by an element-specific experimental technique such as NMR spectroscopy. Fig. 1b shows the ^{39}K NMR spectra for the $K_xCs_{3-x}C_{60}$ series (with refined x_K varying between 0.53 and 3) at ambient temperature. For disorder-free K_3C_{60} ($x = 3$), sharp peaks of both O- and T-lattice-sites can be clearly recognized.[24] On the other hand, the O-site peak is completely suppressed for K_2CsC_{60} ($x_K = 2$), implying preferential occupation of the O site by the larger Cs^+ ion with K^+ residing in the T cavities. This trend persists as x becomes smaller, albeit with the observation of a significantly broadened T-site ^{39}K NMR peak (Fig. S4†). This is the signature of increased cation disorder due to the random distribution of the differently sized K^+ and Cs^+ cations amongst the T-sites of the fcc lattice (vide infra).

Rietveld analysis of the ambient-temperature data (Fig. 2, S5–S11 and Table S1†) was therefore undertaken by incorporating the information from NMR spectroscopy – K^+ ions were only included in the T sites while, for $x < 2$, Cs^+ ions were allowed to occupy both T and O sites. Across the $K_xCs_{3-x}C_{60}$ series, we find that the lattice constants of the cubic phases with fcc symmetry decrease monotonically as the K content
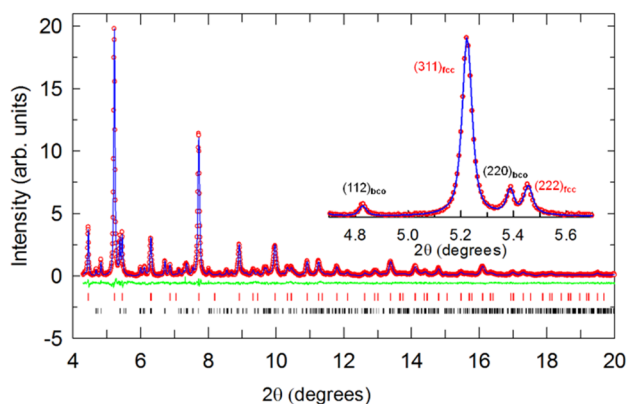

Fig. 2 Rietveld refinement of the synchrotron XRPD data collected at 300 K for fcc-structured $K_xCs_{3-x}C_{60}$ with refined K-content, $x_K = 0.87(1)$ ($\lambda = 0.39984$ Å). Red circles, blue lines and green lines represent the observed, calculated and difference profiles, respectively. Ticks mark the reflection positions of the fcc (85.18(7)%, red) and the body-centred-orthorhombic (bco) Cs_4C_{60} (14.8(1)%, black) phases. Inset: expanded view in the range 4.7° to 5.7° with reflections labelled by their hkl Miller indices.
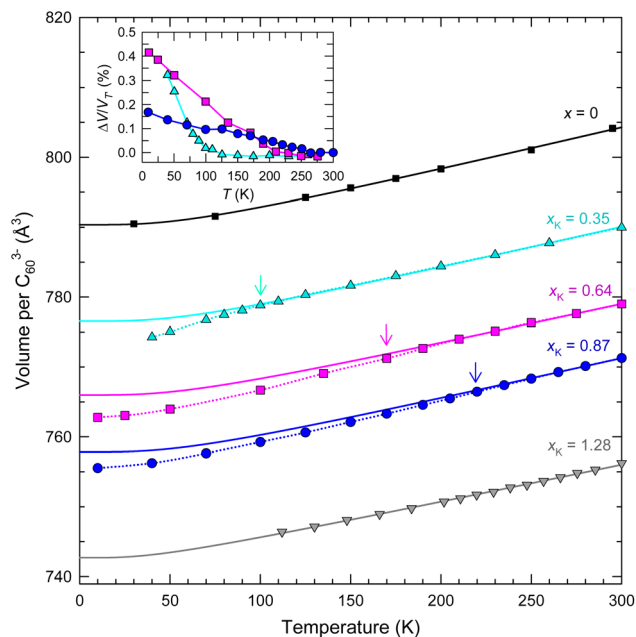
increases. At the same time, the refined stoichiometry of the fcc phase in each sample and the composition of the phase assemblage were determined. The refined stoichiometries differ from the nominal ones, except for the $x = 2$ sample, with the refined K-content, x_K being consistently higher than the nominal value. At the same time, the refined fcc phase fractions increase from 31.5(2)% (the remaining comprising Cs_4C_{60} and CsC_{60}) for the most expanded phase, $x_K = 0.22(1)$ to 94.05(1)% for $x_K = 1.626(4)$ and 100% for $x_K = 1.996(6)$. The results are summarized in Tables S2–S9.† Fig. S12† shows that the fcc lattice parameter, a varies linearly with the refined K content, x_K across the $K_xCs_{3-x}C_{60}$ series in agreement with Vegard's law and confirming the random distribution of the K^+ and Cs^+ alkali ions amongst the lattice T-sites. Notably the slope $da/dx_K = -0.234(3)$ Å is significantly larger than that determined for the $Rb_xCs_{3-x}C_{60}$ analogues ($da/dx_{Rb} = -0.150(4)$ Å (ref. 11)), as expected by the smaller ionic size of K^+ than that of the Rb^+ intercalant.

The temperature dependence of the fcc crystal structures of the members of the $K_xCs_{3-x}C_{60}$ series with $x_K = 0.35$, 0.64, 0.87, and 1.28, as studied by SXRPD, shows that the cubic structure is robust and survives to the lowest temperature of the present experiments. In particular, the thermal behaviour of the unit cell volume of the $K_xCs_{3-x}C_{60}$ composition with a high K-content, $x_K = 1.28$ mimics that of the parent Cs_3C_{60} (ref. 4) showing a smooth lattice contraction on cooling that can be accounted for with a Debye–Grüneisen model (see the corresponding text in the ESI† for details of the Debye–Grüneisen analysis).[25] On the other hand, the contraction of the unit cell volume of the compositions with $x_K = 0.35$, 0.64, and 0.87 with decreasing temperature is not smooth and exhibits an anomalous reduction, ΔV from the value derived from the Debye–Grüneisen fits below a characteristic temperature, $T' \sim 97$, 170, and 220 K, respectively (Fig. 3 and Table S10†). The normalised volume changes, $\Delta V/V_{T'}$ range between 0.2 and 0.4% (inset Fig. 3). Rietveld refinements (Fig. S13–S16, Tables S4–S6 and S8†) establish the isosymmetric nature of the structure across the observed anomalies in the lattice metrics. In a similar fashion to the $V(T)$ response of the $Rb_xCs_{3-x}C_{60}$ ($0.25 \leq x \leq 1.5$) analogues,[11,14] T' shifts to higher temperatures and the anomalous behaviour extends over a larger temperature range as the lattice contracts with increasing K content, x_K.

The pressure dependence of the low-temperature crystal structures of the three $K_xCs_{3-x}C_{60}$ samples with $x_K = 0.35$, 0.87 and 1.28 was also followed by SXRPD to 10 GPa at 7 K. Rietveld analysis of the diffraction profiles confirms the robustness of the fcc structure under the high-pressure conditions too (Fig. S17–S19 and Tables S11–S13†). Fits of the non-linear pressure dependence of the 7 K unit cell volume to the semi-empirical second-order Murnaghan equation-of-state (EoS)[26] for each composition (Fig. S20†) allow us to extract the values of the zero-pressure isothermal bulk moduli, K_0 ($\sim$18–19 GPa) and their pressure derivatives, K_0' ($\sim$ 9). These, and the resulting low-temperature volume compressibilities, κ ($\sim$0.05 GPa^{-1}) are comparable to those derived before for fcc-structured Cs_3C_{60} (ref. 4) and the $Rb_xCs_{3-x}C_{60}$ analogues[11] (Table S14†).

Fig. 3 Temperature evolution of volume, V, occupied per C_{60}^{3-} anion for fcc-structured $K_xCs_{3-x}C_{60}$ samples with $x_K = 0.35$, 0.64, 0.87 and 1.28 and for Cs_3C_{60}.[4] The arrows mark the onset temperatures of the change in lattice response, denoted T', where present. The solid lines through the data are Debye−Grüneisen fits[25] for $T > T'$ (or over all T for $x = 0$ and $x_K = 1.28$) (Table S10†). The dotted lines through the data at $T < T'$ are guides to the eye. Inset: temperature dependence of the normalised volume change, $\Delta V/V_{T'}$ for $x_K = 0.35$, 0.64 and 0.87 − ΔV is the difference in volume between that predicted by the Debye−Grü-neisen fits and that derived experimentally. The errors in V per C_{60}^{3-} from Rietveld analysis are smaller than the size of the data points.

3.2 Electronic properties of $K_xCs_{3-x}C_{60}$ at ambient and elevated pressures

The superconducting properties of the $K_xCs_{3-x}C_{60}$ samples (x_K content in the range between 0.22 and 2) at ambient pressure were investigated by low-field magnetization measurements. Bulk superconductivity is observed with T_c initially increasing from 26.5 K in overexpanded $K_{0.22}Cs_{2.78}C_{60}$ (shielding fraction 16%) to 30.9 K in optimally expanded $K_{0.87}Cs_{2.13}C_{60}$ (40%) and then decreasing to 22.8 K in underexpanded K_2CsC_{60} (52%) (Fig. 4a, b and S21†). The variation of T_c with K content in fcc $K_xCs_{3-x}C_{60}$ mimics the $T_c(V)$ behaviour of fcc Cs_3C_{60} (ref. 4) and the $T_c(V)$ and $T_c(x)$ behaviour of isostructural $Rb_xCs_{3-x}C_{60}$,[11] displaying well-defined dome shape (Fig. 4c). At large unit cell volumes – *i.e.* at low co-doping levels of K^+ or Rb^+ – there is little change in T_c at fixed lattice sizes between the $K_xCs_{3-x}C_{60}$ and $Rb_xCs_{3-x}C_{60}$ systems. However, at small unit cell volumes as the amount of the K^+ or Rb^+ co-dopants in the tetrahedral inter-stices increases, T_c is markedly suppressed in the $K_xCs_{3-x}C_{60}$ family relative to those in $Rb_xCs_{3-x}C_{60}$ (maximum T_c at 33.2 K) and pressurized Cs_3C_{60} (maximum T_c at 35.1 K).

The superconducting properties of the materials were also investigated by magnetization measurements, $M(T)$ as a function of both chemical and physical pressure (to ∼10.3 kbar) (Fig. S22†). For the most expanded sample studied,
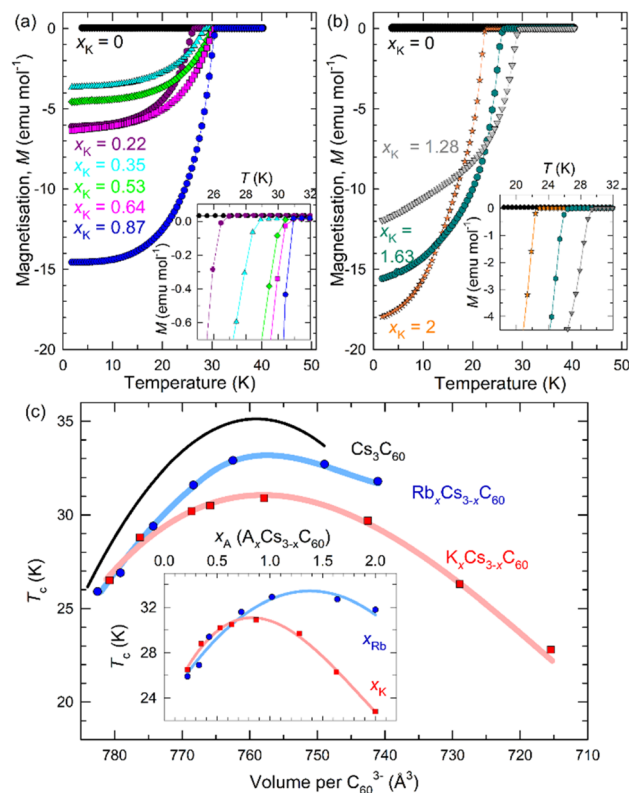

Fig. 4 Temperature dependence of the ZFC magnetisation, M, of the $K_xCs_{3-x}C_{60}$ samples divided by the applied magnetic field. (a) Samples with K-content, $0.22 \leq x_K \leq 0.87$. (b) Samples with K-content, $1.28 \leq x_K \leq 2$. The insets show expanded regions of the respective $M(T)$ data near the superconducting T_c. (c) Variation of ambient pressure superconducting T_c with volume, V occupied per C_{60}^{3-} anion at $T = T_c$ for $K_xCs_{3-x}C_{60}$ ($0.22 \leq x_K \leq 2$) and for $Rb_xCs_{3-x}C_{60}$ ($0.22(1) \leq x_{Rb} \leq 2$)[11,14] together with that for fcc Cs_3C_{60} under pressure.[4] Volumes per C_{60}^{3-} for $K_xCs_{3-x}C_{60}$ at T_c are estimated by extrapolation of the unit cell volumes determined from low-temperature structural data. The inset shows the dependence of T_c on x_K (red squares) and x_{Rb} (blue circles). All solid lines through the data points are guides-to-the-eye.

$K_{0.35}Cs_{2.65}C_{60}$, T_c increases with increasing pressure with an initial pressure coefficient, $(dT_c/dP)_{P=0} = +1.5(2)$ K kbar^{-1}. As x_K increases, the rate of change rapidly decreases, approaching zero for the $K_{0.87}Cs_{2.13}C_{60}$ composition, which shows the highest T_c at ambient pressure. $(dT_c/dP)_{P=0}$ then becomes negative upon further chemical pressurization ($-0.88(1)$ K kbar^{-1} for $K_{1.28}Cs_{1.72}C_{60}$, $-0.99(3)$ K kbar^{-1} for K_2CsC_{60}). Further increase in pressure leads to superconductivity domes for the $0.35 \leq x_K \leq 0.87$ compositions while T_c of the $1.28 \leq x_K \leq 2$ compositions decreases smoothly (Fig. 5a). The variation of the super-conducting T_c of $K_xCs_{3-x}C_{60}$ ($0.35 \leq x \leq 2$) with unit cell volume, V, at low temperature extracted using the $T_c(P)$ data together with 7 K $V(P)$ data (Fig. S20†) is shown in Fig. 5b – the $T_c(V)$ domes show maxima in the vicinity of 760 Å^3 per C_{60}^{3-} in a comparable fashion to the behaviour of pressurized fcc-structured Cs_3C_{60} and $Rb_xCs_{3-x}C_{60}$.

Paramagnetic susceptibility measurements, $\chi(T)$, as a function of temperature at ambient pressure in the normal state have proven before[3,4,11] to be an excellent probe of the electronic
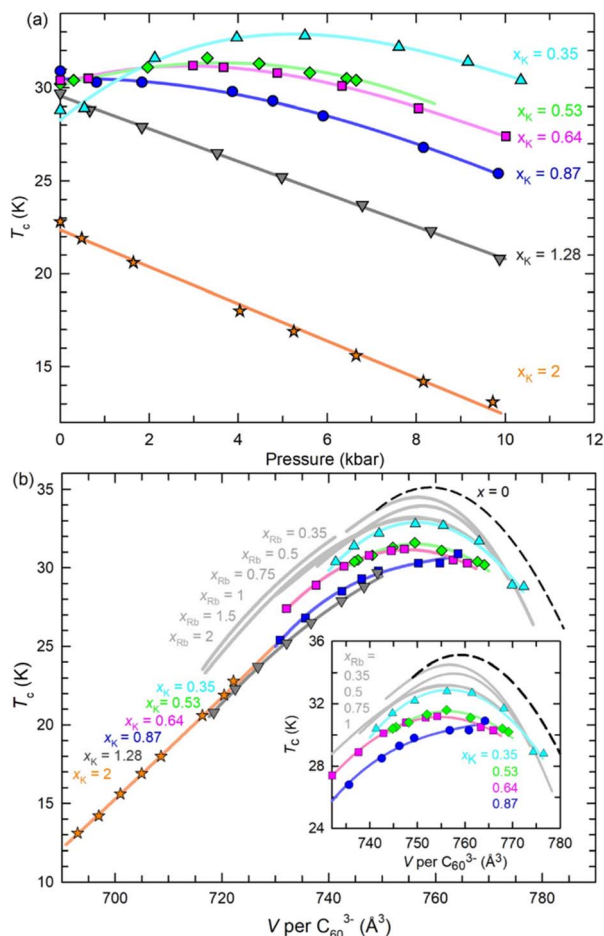
Fig. 5 (a) Variation of the superconducting critical temperature, T_c with pressure for fcc-structured $K_x Cs_{3-x} C_{60}$ ($0.35 \leq x_K \leq 2$). Solid lines through data points are guides to the eye except those for $x_K = 1.28$ and 2 that represent linear fits to the data. (b) Variation of T_c with volume, V, occupied per C_{60}^{3-} anion at low temperature for fcc-structured $K_x Cs_{3-x} C_{60}$ ($0.35 \leq x \leq 2$), $Rb_x Cs_{3-x} C_{60}$ ($0.35 \leq x \leq 2$) (grey solid lines) and $Cs_3 C_{60}$ (dashed black line). Solid lines through x_K data points are guides-to-the-eye. The inset shows an expanded view of dome-shaped T_c (V) data.

properties of fullerides, sensitively tracking the insulator-to-metal crossover associated with the lattice anomalies evident in diffraction for selected compositions (*vide supra*). However, $\chi(T)$ data for the present $K_x Cs_{3-x} C_{60}$ phase assemblages at small x_K suffer from also incorporating significant impurity-phase contributions to the measured susceptibility. As a result, well-defined cusps on cooling that provide evidence for insulator-to-metal crossover are hard to ascertain – there is only some weak evidence of maxima in $\chi(T)$ at ~68 and 97 K for $K_{0.22} Cs_{2.78} C_{60}$ and $K_{0.35} Cs_{2.65} C_{60}$, respectively (Fig. S23†). The $\chi(T)$ data for moderately expanded compositions with $x_K = 0.53$ and 0.64 no longer display any cusps but they do not exhibit a temperature-independent Pauli susceptibility term either. Such a term, which is consistent with a metallic ground state from which superconductivity emerges on cooling, appears to be present for underexpanded compositions with $x_K = 1.28$ and 2.

Given the ambiguities associated with the $\chi(T)$ datasets due to the multiphase nature of the samples, we used the local-probe NMR technique to follow the temperature evolution of the electronic properties of the $K_{0.64} Cs_{2.36} C_{60}$ composition. The ^{133}Cs spin-lattice relaxation rate divided by temperature, $1/^{133}T_1 T$, which measures the imaginary part of the dynamic electron spin susceptibility, provides a sensitive insight into the electronic degrees of freedom as they develop across the insulator-to-metal crossover.[3,4,11] On cooling from high temperatures, $1/^{133}T_1 T$ for both O- and T-sites of $K_{0.64} Cs_{2.36} C_{60}$ slightly increases with decreasing temperature (see Fig. S24† and the corresponding text in the ESI† for details of the spectral and ^{133}Cs relaxation rate analysis) showing qualitatively comparable behaviour to that previously observed in $RbCs_2 C_{60}$ and in Mott-insulating low-spin ($S = \frac{1}{2}$) $Cs_3 C_{60}$ (ref. 4, 11 and 14) (Fig. 6). Consistent with the structural results, $1/^{133}T_1 T$ of $K_{0.64} Cs_{2.36} C_{60}$ begins to decrease below $T' \sim 170$ K, as expected for a crossover to a Jahn–Teller metal[11] and in close similarity with the behaviour of $RbCs_2 C_{60}$. Above T', the $1/^{133}T_1 T$ datasets for the two samples with comparable unit-cell volumes show different dependences with increasing temperature with the difference increasing as we move away from the insulator-to-metal crossover line. This implies the existence of another control parameter, namely interstitial site disorder (*vide infra*), which further controls the local electronic properties.

Below $T_c = 27$ K (the value of the critical temperature in the NMR magnetic field of 9.39 T), $1/^{133}T_1 T$ of $K_{0.64} Cs_{2.36} C_{60}$ is suddenly suppressed indicating the opening of a super-conducting gap, Δ, while at the same time, no Hebel–Slichter coherence peak is observed. The spin-lattice relaxation rate adopts a thermally activated dependence $1/^{133}T_1 \propto \exp[-\Delta_0/k_B T]$, in agreement with an isotropic s-wave superconducting gap (Fig. S25†). The semilog plot allows us to extract an estimate of the superconducting gap, Δ_0. The normalized gap value, $2\Delta_0/$
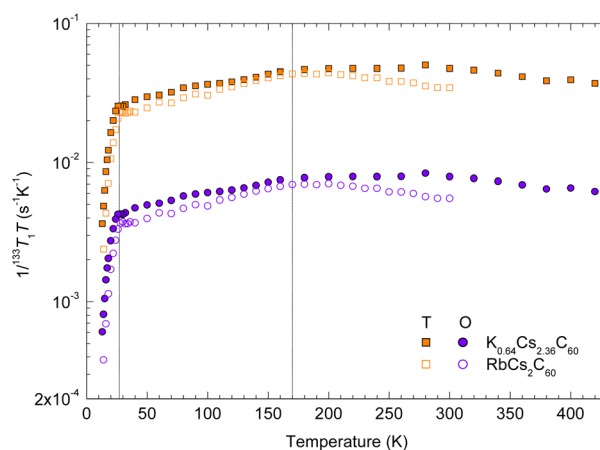

Fig. 6 Temperature dependence of the ^{133}Cs spin-lattice relaxation rates divided by temperature, $1/^{133}T_1 T$ for $K_{0.64} Cs_{2.36} C_{60}$ (solid symbols) and for similarly expanded $RbCs_2 C_{60}$ (open symbols) from ref. 11. In both cases, squares and circles mark the data for T- and O-sites, respectively. The dotted lines mark the temperature, T' at which maxima in $1/^{133}T_1 T$ are observed and the onset of superconductivity at T_c in the NMR magnetic field of 9.39 T.

$k_BT_c \sim 5$ is significantly enhanced relative to that of a weakly coupled BCS superconductor ($2\Delta_0/k_BT_c = 3.52$) in a similar fashion to the behaviour of the overexpanded members of the $Rb_xCs_{3-x}C_{60}$ family.[11]

4 Discussion

The electronic phase diagram of selected fcc-structured A_3C_{60} fullerides was mapped out in the past both by the application of physical pressure to the highly expanded MJTI Cs_3C_{60} phase[4,13] and of chemical pressure in the series of $Rb_xCs_{3-x}C_{60}$ ($0 \leq x \leq 2$) compositions in which Cs^+ is quasi-continuously replaced by the smaller Rb^+ cation.[11,14,27] The $K_xCs_{3-x}C_{60}$ ($0 \leq x \leq 2$) phases investigated here are direct analogues of their antecedents in the $Rb_xCs_{3-x}C_{60}$ ($0 \leq x \leq 2$) series with the smaller K^+ ion being now employed as a direct substituent of Cs^+. The fcc unit cell size decreases again linearly with increasing content of the smaller K^+ ion (Fig. S12†), thereby permitting the exploration of the electronic properties of the $K_xCs_{3-x}C_{60}$ ($0 \leq x \leq 2$) fullerides across a broad region of the phase diagram from under-expanded to overexpanded *via* optimally expanded compositions. The existence of a superconductivity dome and the presence of a crossover of the normal metallic state from a correlated JT metal to a Fermi liquid, as the packing density of the fulleride units decreases are essentially identical observations to those established before for the fcc $Rb_xCs_{3-x}C_{60}$ compounds.[11,14] However, a noticeable difference in behaviour of the $K_xCs_{3-x}C_{60}$ ($0 \leq x \leq 2$) compositions, as evidenced in Fig. 4c and 5b, is the presence of a significant suppression of the superconducting transition temperature, T_c when compared with the values measured in both $Rb_xCs_{3-x}C_{60}$ and pressurised Cs_3C_{60} at the same packing densities, $V/C_{60}{}^{3-}$.

In order to understand the origin of the suppression of T_c in the $K_xCs_{3-x}C_{60}$ series, we first examine the variation of the packing density, $V/C_{60}{}^{3-}$ with the average radius of the ions occupying the tetrahedral sites, $\langle r_{A,T} \rangle$ (A = K, Rb, Cs). Fig. S26† shows that the identity of the ions themselves is important in determining the packing density. As the amount of the K^+ or Rb^+ co-intercalants into the tetrahedral sites of the Cs_3C_{60} structure increases by partially replacing the larger Cs^+ ions, the packing density smoothly decreases. However, the rate of decrease is distinctly different between the $K_xCs_{3-x}C_{60}$ ($dV/d\langle r_{A,T} \rangle = 250(3)$ Å^2) and the $Rb_xCs_{3-x}C_{60}$ ($dV/d\langle r_{A,T} \rangle = 306(9)$ Å^2) series. This leads to an increasing deviation between their corresponding $V/C_{60}{}^{3-}$ *vs.* $\langle r_{A,T} \rangle$ lines at the same average ionic size for large co-intercalant content (Fig. S26†). It is an indication of the potential importance of disorder in the tetrahedral sites – that arises from the difference in size mismatch between the inter-calants, namely $(r_{Cs^+} - r_{K^+}) > (r_{Cs^+} - r_{Rb^+})$ – on the structural and electronic properties of the materials.

The degree of cation disorder may be quantified by the magnitude of the statistical variance, $\sigma_T{}^2$ in the distribution of the T-site ionic radii, namely $\sigma_T{}^2 = \sum x_{A,T} r_{A,T}{}^2 - \langle r_{A,T} \rangle^2$. The inset in Fig. S26† shows the variation in cation disorder with the average cation radius, $\langle r_{A,T} \rangle$ of the tetrahedral sites for both $K_xCs_{3-x}C_{60}$ and $Rb_xCs_{3-x}C_{60}$. The magnitude of $\sigma_T{}^2$ gradually increases as we replace Cs^+ with K^+ or Rb^+ ions at the T-sites of

fcc-structured Cs_3C_{60}. In both cases, it reaches a maximum value and then decreases, producing a dome-shaped scaling of cation size variance with $\langle r_{A,T} \rangle$. The degree of cation disorder is significantly larger in the case of the K^+ co-intercalant for the $K_xCs_{3-x}C_{60}$ series whereas it is absent in the parent Cs_3C_{60} and A_2CsC_{60} (A = K, Rb) phases for which $\sigma_T{}^2 = 0$.

The static local structural disorder quantified by $\sigma_T{}^2$ is directly associated with the elastic strain whose fluctuations affect critical temperatures. Returning to Fig. 5b, which displays the values of superconducting T_c for fcc Cs_3C_{60} under pressure together with those for $Rb_xCs_{3-x}C_{60}$ and $K_xCs_{3-x}C_{60}$ at ambient pressure *vs.* the packing density of the fulleride units, it is apparent that there are three distinct domes peaking roughly at comparable values of $V/C_{60}{}^{3-}$ but displaced vertically – one for each family. The highest value of the measured T_cs at each V is encountered for pressurized Cs_3C_{60}, followed by that for $Rb_xCs_{3-x}C_{60}$, and then by that for $K_xCs_{3-x}C_{60}$. For instance, $(T_c)_{max}$ for the $K_xCs_{3-x}C_{60}$ ($x_K = 0.87$, $V = 757.9$ Å^3) composition at ambient pressure at the top of the dome is 30.9 K. For the same lattice size of the fulleride salts, T_c increases first to 33.2 K at ambient pressure for the $Rb_xCs_{3-x}C_{60}$ family and then to 35.1 K for pressurized Cs_3C_{60}, an overall increase of 4.2 K. This trend is associated with a decrease in the value of the T-site cation size variance, $\sigma_T{}^2$ from 0.021 Å^2 (in the K-substituted series) to 0.005 Å^2 (in the Rb-substituted series) to 0 Å^2 (in pressurized Cs_3C_{60}). Fig. 7 displays the variation of the T_c suppression, $\Delta T_c = T_c(Cs_3C_{60}) - T_c(K_xCs_{3-x}C_{60}, P = 1 \text{ atm})$ with $\sigma_T{}^2$ and with packing density, $V/C_{60}{}^{3-}$ as an implicit parameter for

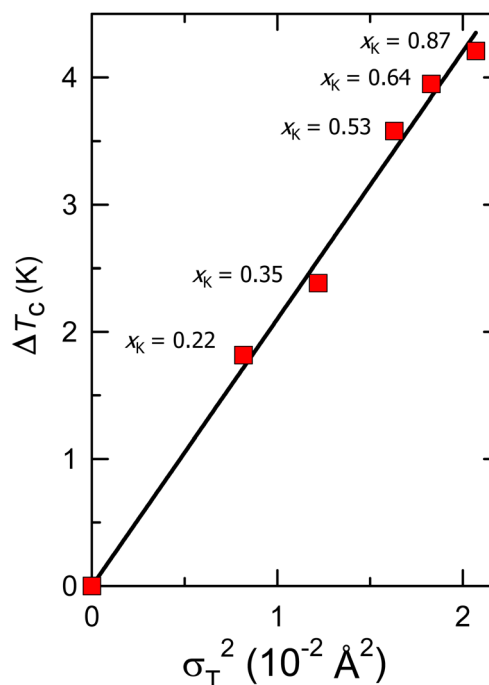
Fig. 7 Dependence of the suppression of the ambient-pressure superconducting T_c of the $K_xCs_{3-x}C_{60}$ ($0.22 \leq x_K \leq 0.87$) compounds relative to that of the pressurized binary analogue, Cs_3C_{60} at the same C_{60} packing density on the tetrahedral-site cation size variance. The solid red line is a linear fit to the data.

compositions lying at the maximum and on the overexpanded side of the superconductivity dome. ΔT_c varies linearly with σ_T^2 with a slope of $d\Delta T_c/d\sigma_T^2 = 210(4)$ K Å^{-2}, thus demonstrating a clear link between T-site disorder of the electronically inactive alkali ions and suppression of T_c.

Such effects have attracted considerable interest before in other classes of strongly correlated materials, namely perovskite transition-metal oxides. For instance, it was demonstrated that the metal-to-insulator transition temperature in colossal magnetoresistive manganites, $(RE_{1-x}AE_x)MnO_3$ responds sensitively to changes in lattice strain associated with the variation in ionic size mismatch of the electronically inactive rare earth (RE) and alkaline earth (AE) supporting cations.[20,28] In a similar fashion, the superconducting T_c in high-temperature cuprate superconductors, $(RE_{1-x}AE_x)_2CuO_4$ decreases linearly with increasing disorder of the supporting cation site arising from differences in size between the rare earth and alkaline earth cations.[21,29] Similar observations of the importance of ionic size disorder effects in controlling the onset of phase transitions have been also made for nickelates,[30] titanates,[31] and ferroelectrics.[32] Theoretically the large effect of ionic size disorder on Mott-like phase transitions has been understood in terms of dynamic fluctuations of the resulting elastic strain as demonstrated in statistical mechanical models, which incorporate cooperative lattice distortions coupled explicitly to the electronic degrees of freedom.[19] Thus it appears that comparable strong elastic interactions are also relevant in strongly correlated molecular systems such as the fcc-structured alkali fullerides, $(A_{1-x}A'_x)_3C_{60}$. Here the onset of superconductivity is shown to be tunable not only by purely electronic effects associated with the fulleride sublattice – as quantified by the (U/W) ratio – but also by elastic strain effects – as quantified by the variance in the distribution of the radii of the supporting A and A′ cations residing in the T-sites of the fcc structure.

5 Conclusions

In conclusion, we have investigated in detail the structural and electronic properties of the series of fcc-structured $K_xCs_{3-x}C_{60}$ fullerides ($0.22 \leq x_K \leq 2$) by means of SXRPD, NMR spectroscopy, and SQUID magnetometry at both ambient and elevated pressures. High-resolution synchrotron XRPD shows that there are no structural phase transitions occurring for any of the compositions studied at all temperatures and pressures investigated. Insulator-to-metal crossovers are encountered on cooling at ambient pressure, evident by both a lattice size decrease without an accompanying crystal symmetry change and a maximum in the $1/^{133}T_1T$ vs. T ^{133}Cs NMR spin lattice relaxation data. Composition-dependent T_c measurements at both ambient and elevated pressures reproduce dome-shaped responses to changes in the fulleride packing density.

At the same time, the results permit the extension of the electronic phase diagram of the fcc-structured A_3C_{60} fullerides to compositions with significantly increased chemical disorder, as quantified by the statistical variance, σ_T^2 in the distribution of tetrahedral-site ionic radii. We establish a very sensitive dependence of T_c on the lattice strains associated with the

cation size variance at the same packing density, V/C_{60}^{3-} – the suppression of T_c from its value in the absence of disorder varies linearly with lattice strains at a rate of 210(4) K Å^{-2}.

Data availability

All the necessary data to support the findings of this study can be found within the main text and ESI.†

Author contributions

Synthesis, H. E. O. and R. H. C.; synchrotron X-ray diffraction—data collection and analysis, H. E. O., R. H. C., Y. T., K. K., and K. P.; high-pressure synchrotron X-ray diffraction—data collection and analysis, H. E. O., R. H. C., Y. T., Y. O., and K. P.; NMR spectroscopy, P. J. and D. A.; conceptualization and overall conclusions, D. A., Y. K., and K. P.; project supervision, K. P.; writing—review and editing, D. A. and K. P. All authors have read and agreed to the published version of the manuscript.

Conflicts of interest

There are no conflicts to declare.

Acknowledgements

Notes and references

1 A. Y. Ganin, Y. Takabayashi, Y. Z. Khimyak, S. Margadonna, A. Tamai, M. J. Rosseinsky and K. Prassides, *Nat. Mater.*, 2008, **7**, 367–371.

2 Y. Kasahara, Y. Takeuchi, R. H. Zadik, Y. Takabayashi, R. H. Colman, R. D. McDonald, M. J. Rosseinsky, K. Prassides and Y. Iwasa, *Nat. Commun.*, 2017, **8**, 14467.

3 Y. Takabayashi, A. Y. Ganin, P. Jeglic, D. Arcon, T. Takano, Y. Iwasa, Y. Ohishi, M. Takata, N. Takeshita, K. Prassides and M. J. Rosseinsky, *Science*, 2009, **323**, 1585–1590.

4 A. Y. Ganin, Y. Takabayashi, P. Jeglič, D. Arčon, A. Potočnik, P. J. Baker, Y. Ohishi, M. T. McDonald, M. D. Tzirakis, A. McLennan, G. R. Darling, M. Takata, M. J. Rosseinsky and K. Prassides, *Nature*, 2010, **466**, 221–227.

5 M. Capone, M. Fabrizio, C. Castellani and E. Tosatti, *Rev. Mod. Phys.*, 2009, **81**, 943–958.

6 Y. Nomura, S. Sakai, M. Capone and R. Arita, *Sci. Adv.*, 2015, **1**, e1500568.

7 S. Hoshino and P. Werner, *Phys. Rev. Lett.*, 2017, **118**, 177002.

8 Y. Takabayashi and K. Prassides, *Philos. Trans. R. Soc., A*, 2016, **374**, 20150320.

9 H. Alloul, P. Wzietek, T. Mito, D. Pontiroli, M. Aramini, M. Riccò, J. P. Itie and E. Elkaim, *Phys. Rev. Lett.*, 2017, **118**, 237601.

10 Y. Ihara, H. Alloul, P. Wzietek, D. Pontiroli, M. Mazzani and M. Ricco, *Phys. Rev. Lett.*, 2010, **104**, 256402.

11 R. H. Zadik, Y. Takabayashi, G. Klupp, R. H. Colman, A. Y. Ganin, A. Potocnik, P. Jeglic, D. Arcon, P. Matus, K. Kamaras, Y. Kasahara, Y. Iwasa, A. N. Fitch, Y. Ohishi, G. Garbarino, K. Kato, M. J. Rosseinsky and K. Prassides, *Sci. Adv.*, 2015, **1**, e1500059.

12 Y. Takabayashi and K. Prassides, *Struct. Bonding*, 2016, **172**, 119–138.

13 R. H. Zadik, Y. Takabayashi, R. H. Colman, G. Garbarino and K. Prassides, *Mater. Chem. Front.*, 2018, **2**, 993–998.

14 M. Menelaou, Y. Takabayashi, H. E. Okur, R. H. Zadik and K. Prassides, *Int. J. Mod. Phys. B*, 2018, **32**, 1840020.

15 G. Klupp, P. Matus, K. Kamarás, A. Y. Ganin, A. McLennan, M. J. Rosseinsky, Y. Takabayashi, M. T. McDonald and K. Prassides, *Nat. Commun.*, 2012, **3**, 912.

16 P. Wzietek, T. Mito, H. Alloul, D. Pontiroli, M. Aramini and M. Ricco, *Phys. Rev. Lett.*, 2014, **112**, 066401.

17 A. Potočnik, A. Krajnc, P. Jeglič, Y. Takabayashi, A. Y. Ganin, K. Prassides, M. J. Rosseinsky and D. Arčon, *Sci. Rep.*, 2014, **4**, 4265.

18 A. Potocnik, A. Y. Ganin, Y. Takabayashi, M. T. McDonald, I. Heinmaa, P. Jeglic, R. Stern, M. J. Rosseinsky, K. Prassides and D. Arcon, *Chem. Sci.*, 2014, **5**, 3008–3017.

19 G. G. Guzman-Verri, R. T. Brierley and P. B. Littlewood, *Nature*, 2019, **576**, 429–432.

20 L. M. Rodriguez-Martinez and J. P. Attfield, *Phys. Rev. B: Condens. Matter Mater. Phys.*, 1996, **54**, R15622–R15625.

21 J. P. Attfield, A. L. Kharlanov and J. A. McAllister, *Nature*, 1998, **394**, 157–159.

22 K. Kato and H. Tanaka, *Adv. Phys.: X*, 2016, **1**, 55–80.

23 A. C. Larson and R. B. Von Dreele, *General Structure Analysis System (GSAS) Report LAUR 86-748*, Los Alamos National Laboratory, 2004.

24 Y. Yoshinari, H. Alloul, V. Brouet, G. Kriza, K. Holczer and L. Forro, *Phys. Rev. B: Condens. Matter Mater. Phys.*, 1996, **54**, 6155–6166.

25 F. Sayetat, P. Fertey and M. Kessler, *J. Appl. Crystallogr.*, 1998, **31**, 121–127.

26 F. D. Murnaghan, *Am. J. Math.*, 1937, **59**, 235–260.

27 H. E. Okur and K. Prassides, *J. Phys. Chem. Solids*, 2019, **131**, 44–49.

28 Y. L. Wang, M. F. Liu, R. Liu, Y. L. Xie, X. Li, Z. B. Yan and J.-M. Liu, *Sci. Rep.*, 2016, **6**, 27840.

29 J. A. McAllister and J. P. Attfield, *Phys. Rev. B: Condens. Matter Mater. Phys.*, 2002, **66**, 014514.

30 S. Catalano, M. Gibert, J. Fowlie, J. Iniguez, J.-M. Triscone and J. Kreisel, *Rep. Prog. Phys.*, 2018, **81**, 046501.

31 T. Katsufuji, Y. Taguchi and Y. Tokura, *Phys. Rev. B: Condens. Matter Mater. Phys.*, 1997, **56**, 10145–10153.

32 P. V. Balachandran, S. R. Broderick and K. Rajan, *Proc. R. Soc. A*, 2011, **467**, 2271–2290.